Climate Dynamics (1996) 12:667–683

Climate Dynamics

© Springer-Verlag 1996

Interannual and interdecadal variabilities in the Pacific in an MRI coupled GCM

S. Yukimoto[1], M. Endoh[1], Y. Kitamura[1], A. Kitoh[1], T. Motoi[1], A. Noda[1], T. Tokioka[2]

[1] Meteorological Research Institute, 1-1 Nagamine, Tsukuba, Ibaraki 305, Japan
[2] Japan Meteorological Agency, Tokyo 100, Japan

Received: 6 November 1995 / Accepted: 19 April 1996

Abstract. Interannual and interdecadal variabilities in the Pacific are investigated with a coupled atmosphere-ocean GCM developed at MRI, Japan. The model is run for 70 years with flux adjustments. The model shows interannual variability in the tropical Pacific which has several typical characteristics shared with the observed ENSO. A basin-scale feature of the principal SST variation for the ENSO time scale shows negative correlation in the central North Pacific with the tropical SST, similar to that of the observed one. Associated variation of the model atmosphere indicates an intensification of the Aleutian Low and a PNA-like teleconnection pattern as a response to the tropical warm SST anomaly. The ENSO time scale variability in the midlatitude ocean consists of the westward propagation of the subsurface temperature signal and the temperature variation within the shallow mixed layer forced by the anomalous atmospheric heat fluxes. For the interdecadal time scale, variation of the SST is simulated realistically with a geographical pattern similar to that for the ENSO time scale, but it has a larger relative amplitude in the northern Pacific. For the atmosphere, spatial structure of the variation in the interdecadal time scale is also similar to that in the ENSO time scale, but has smaller amplitude in the northern Pacific. Long oceanic spin-up time ($> \sim 10$ y) in the mid-high latitude, however, makes oceanic response in the interdecadal time scale larger than that in the ENSO time scale. The lagged-regression analysis for the ocean temperature variation relative to the wind stress variation indicates that interdecadal variation of the ocean subsurface at the mid-high latitudes is considered as enhanced ocean gyre spin-up process in response to the atmospheric circulation change at the mid-high latitudes, remotely forced by the interdecadal variation of the tropical SST.

This paper was presented at the Third International Conference on Modelling of Global Climate Change and Variability, held in Hamburg 4–8 Sept. 1995 under the auspices of the Max Planck Institute for Meteorology, Hamburg. Editor for these papers is L. Dümenil.

Correspondence to: S. Yukimoto

1 Introduction

Along with increasing concern about global warming due to anthropogenic greenhouse gases, it has been recognized that a full understanding of the natural variability of the climate system is most essential for quantitative detection of the warming and for reduction of uncertainties in the prediction of future climates. Increasing numbers of experiments with coupled atmosphere-ocean GCMs have been conducted in order to investigate transient responses of climate system to the growth of atmospheric greenhouse gases (e.g. Manabe et al. 1991; Cubash et al. 1992). It is realized that quantitative detection of greenhouse effect is difficult due to the existence of natural variability of interdecadal time scale with comparable amplitude (IPCC 1990). The model's performances need to reproduce realistically natural variability for climate sensitivity experiments. In several transient experiments, interdecadal natural variabilities are simulated in their coupled models (Manabe et al. 1991; Cubash et al. 1992), where resolutions of the ocean models are too low to simulate realistic El Niños.

El Niño and the Southern Oscillation (ENSO) in the tropical Pacific is one of the most dominant interannual natural variabilities of the air-sea coupled system. The influence of ENSO to the midlatitudes was also considered in many observational and GCM investigations.

When considering the natural variability of decadal to interdecadal time scale, on the other hand, the large climate shift in the North Pacific which occurred in the mid-1970s is notable. Kashiwabara (1987) reported a clear decline of winter atmospheric geopotential height in the central North Pacific after 1977. Nitta and Yamada (1989) and Trenberth (1990) pointed out that this change in the atmospheric circulation is related to

decadal scale variation of the tropical ocean. In recent studies with atmospheric GCMs, Lau and Nath (1994) and Graham (1994) forced AGCM by the observed sea surface temperature (SST) in the midlatitude and the tropics separately, and studied contributions of the two SST anomalies to the variability of the midlatitude atmospheric circulations. They suggested that the atmospheric variation in the North Pacific can be attributed to the variation of the tropical Pacific SST. Close linkage between the Aleutian Low and the SST in the western tropical Pacific is also suggested by Yamagata and Masumoto (1992). Miller et al. (1994) showed that interdecadal variability of the midlatitude Pacific Ocean is driven by the atmosphere, from results of an experiment with an OGCM forced by the observed anomalies of surface heat flux and wind stress.

On the other hand, Trenberth and Hurrell (1994) suggested the importance of a feedback mechanism that causes north-south shifts of storm track accompanied by the SST change in the central North Pacific to reinforce or sustain the SST anomaly there. With the analysis of a multi-decadal integration of a coupled GCM, Latif and Barnett (1994) claimed that coupled interaction between the subtropical gyre circulation and the Aleutian Low is also important to interdecadal variability in the North Pacific. In their model, variations in the tropical Pacific are considered of secondary importance to the forcings in the midlatitudes.

An experiment of global warming with transient CO_2 increase is performed at the Meteorological Research Institute (MRI) (Tokioka et al. 1995). The model used for the study has enough resolution in the OGCM in the low latitudes to show ENSO-like variation and interdecadal variation in the Pacific both in the control run and CO_2 increase run. In order to validate the performance of the model, the present study investigates temporal and spatial structures of the simulated variability and compares them with the observation. This work, furthermore, tries to pursue mechanisms of the variabilities in the Pacific with emphasis on the relation between the tropics and the mid-high latitudes.

This study is organized as follows: outlines of the model and the model run are described in Sect. 2. Sections 3 and 4 describe model climatology and overview of the model ENSO, respectively. Sections 5 and 6 describe basin-scale variations in the Pacific for interannual time scales and for interdecadal time scales, respectively. Finally summary and discussion are presented in Sect. 7.

2 Model and run

The coupled atmosphere-ocean model employed in the present study consists of a world ocean general circulation model (OGCM) with an active sea-ice model and an atmospheric general circulation model (AGCM), developed at MRI.

An atmospheric component of the model is a new version of MRI-GCM (Tokioka et al. 1984). Its performance is described in Kitoh et al. (1995). The horizontal resolution of the AGCM is 4° latitude and 5° longitude. There are 15 vertical layers with the model top at 1 hPa. Calculation of the shortwave radiation is based on Lacis and Hansen (1974). Calculation of the longwave radiation is based on the multi-parameter random model by Shibata and Aoki (1989) applied in four spectral regions (20–550, 550–800, 800–1200, 1200–2200 cm^{-1}). Parametrization of cumulus convection is based on the scheme of Arakawa and Schubert (1974). Planetary boundary layer (PBL) is parametrized as a well-mixed layer with variable depth after the model of Randall (1976). Five types of clouds are considered: penetrative cumulus cloud, mid-level convective cloud, stratus cloud in PBL, cloud due to large-scale condensation and cirrus anvil cloud. Partial cloudiness is allowed for the convective clouds. Orographic gravity-wave drag is parametrized following Palmer et al. (1986) with quantitative adjustments by Yagai and Yamazaki (1988). Thermodynamic and hydrological treatment of the land surface are based on a multi-layer soil model which has four layers with the lowest at 10 m depth. Effect of the vegetation canopy is not explicitly modeled. In order to allow different horizontal resolutions between AGCM and OGCM, different types of surface characteristics (ocean, land, sea ice and ice sheet) are considered in a single AGCM grid box.

The oceanic component of the model is a world ocean general circulation model developed at MRI (see Nagai et al. 1992). The model has realistic bottom topography and 2.5° (longitude) × 2.0° (latitude) horizontal resolution. For latitudes lower than 12 degrees, non-uniform latitudinal grid spacing ranges from 0.5° (4°S-4°N) to 2° poleward from 12°N and 12°S). There are 21 vertical levels, 11 of which are located in the upper levels of ocean between deep and the surface 300 m. To resolve the oceanic mixed layer, a turbulence closure scheme based on the Mellor-Yamada level-2 is introduced. Coefficients of the horizontal viscosity and diffusivity are set to 2.0×10^9 cm^2/s and 5.0×10^7 cm^2/s, respectively. The vertical eddy viscosity and diffusivity are calculated following the turbulence closure scheme (Mellor and Yamada 1974, 1982; Mellor and Durbin 1975).

An active sea ice model is included. The model predicts compactness and thickness of sea ice following Mellor and Kantha (1989). Advection of the sea ice is taken into account with a simple relation to the ocean surface current.

The model results analyzed in this study covers a 70-y control run for the transient CO_2 experiment (its atmospheric CO_2 concentration is fixed at 345 ppmv). Before coupling, AGCM was integrated for 3 y forced by the observed SST, and OGCM was spun up for 1500 y from motionless state initially with homogeneous potential temperature and salinity. Then, preliminary coupling 30-y-integration was made, during which flux adjustments of heat and freshwater were obtained through the relaxation of sea surface temperature and salinity to Levitus (1982) climatology. Finally, a 70 y integration was made as a control run. During this inte-

gration, the flux adjustments obtained above were imposed to insure realistic climate of SST and surface salinity.

3 Model climatology

In this section, we overview model climatology of the SST, wind stress, and ocean subsurface thermal structure, compared with observational data.

Annual mean SST climatology for the 70 y integration of the model is shown in Fig. 1. Flux adjustments worked well to maintain the SST close to the Levitus (1982) climatology in the mid-high latitudes as well as in the tropical region. During the 70 y time integration, however, the model has some climatic drift in the subsurface ocean at the high-latitudes especially over the Antarctic sea and the North Atlantic. An overall feature of the SST pattern is reasonably reproduced. Some discrepancies from the observation, however, are seen. The temperature of the western equatorial warm water in the Pacific is slightly higher than 30 °C while the observed one is less than 30 °C. The model SST has generally warm bias in the warm water regions in the tropics.

Figure 2 shows the model climatology of the sea surface wind stress field for (a) January and (b) July. Overall features of the observed wind stress (Hellermann and Rosenstein 1983) are well reproduced. The westerly winds associated with storm tracks in the northern midlatitude and the northeast trade winds are realistic not only in direction but also in amplitude. Since the model Aleutian Low is shifted westward (Fig. 2), the wind stress in the central north Pacific has larger northward component compared to that of the observations. The southeasterly trade winds of the model do not extend to the equator especially in the west off Peru and off Brazil. Generally speaking, the meridional component of the model wind stress in the tropics is small compared to that observed. In July (Fig. 2b), the strong southwesterly wind stress which is related to the Indian monsoon is reasonably simulated.

In order to simulate realistic El Niños, it is crucial that the thermocline along the equator is adequately reproduced. Both the annual mean field and seasonal variation of wind stress along the equator are closely tied to the thermocline structure along the equator. Figure 3 shows the seasonal variation of the zonal wind stress and the meridional wind stress both along the equator. These are compared with the observational wind stress of Hellermann and Rosenstein (1983). In the comparison, the observational wind stress of Hellermann and Rosenstein (1983) is multiplied by 0.75, because it is considered to be overestimated (Stockdale et al. 1993). In January, zonal wind stress in the model shows good agreement with the observations. In April, the observed easterly wind stress is weakened in the central Pacific, although the model maintains easterly wind stress at January values. The model simulates the easterly wind stress in the central equatorial Pacific

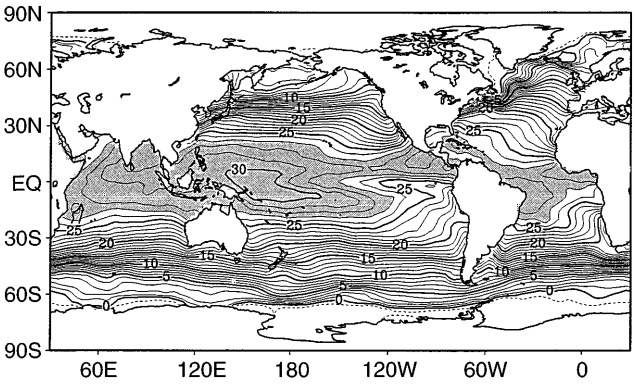

Fig. 1. Model climatology of the annual averaged SST. Contour interval is 1 °C. Regions warmer than 27 °C are *shaded*

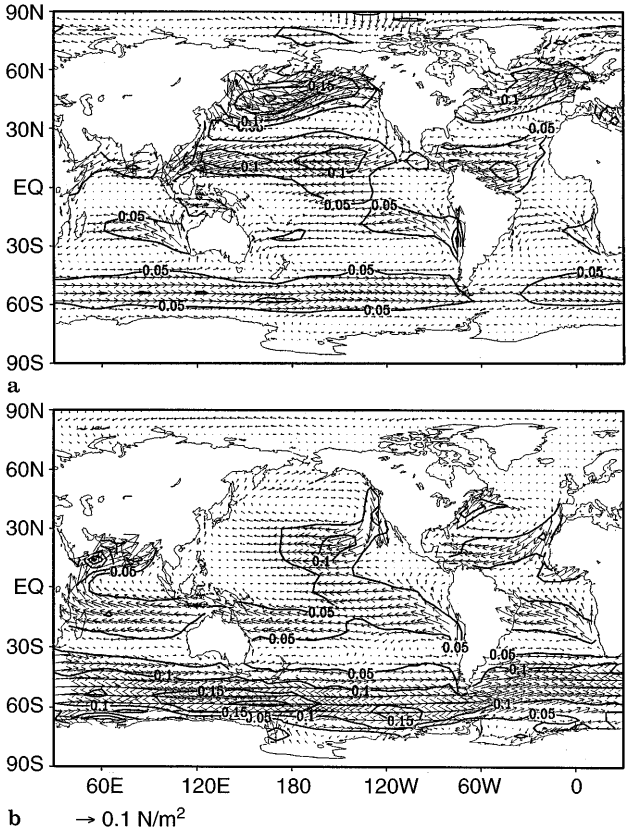

Fig. 2a, b. Model climatology of the wind stress at the ocean surface for **a** January and **b** July. *Reference arrow* denotes 0.1 N/m^2. *Contour plot* shows magnitude of wind stress with interval of 0.05 N/m^2

to be about 50% larger than that observed during April through July. The zonal wind stress in the eastern coast of the Pacific in the model has a relatively large westerly component compared to observations. Meridional wind stress plays significant role in coastal upwelling and cold currents along the eastern coast of the Pacific and the Atlantic. Southerly wind stresses in the model are weak compared to observations in the equatorial east-central Pacific and Atlantic especially during July to October.

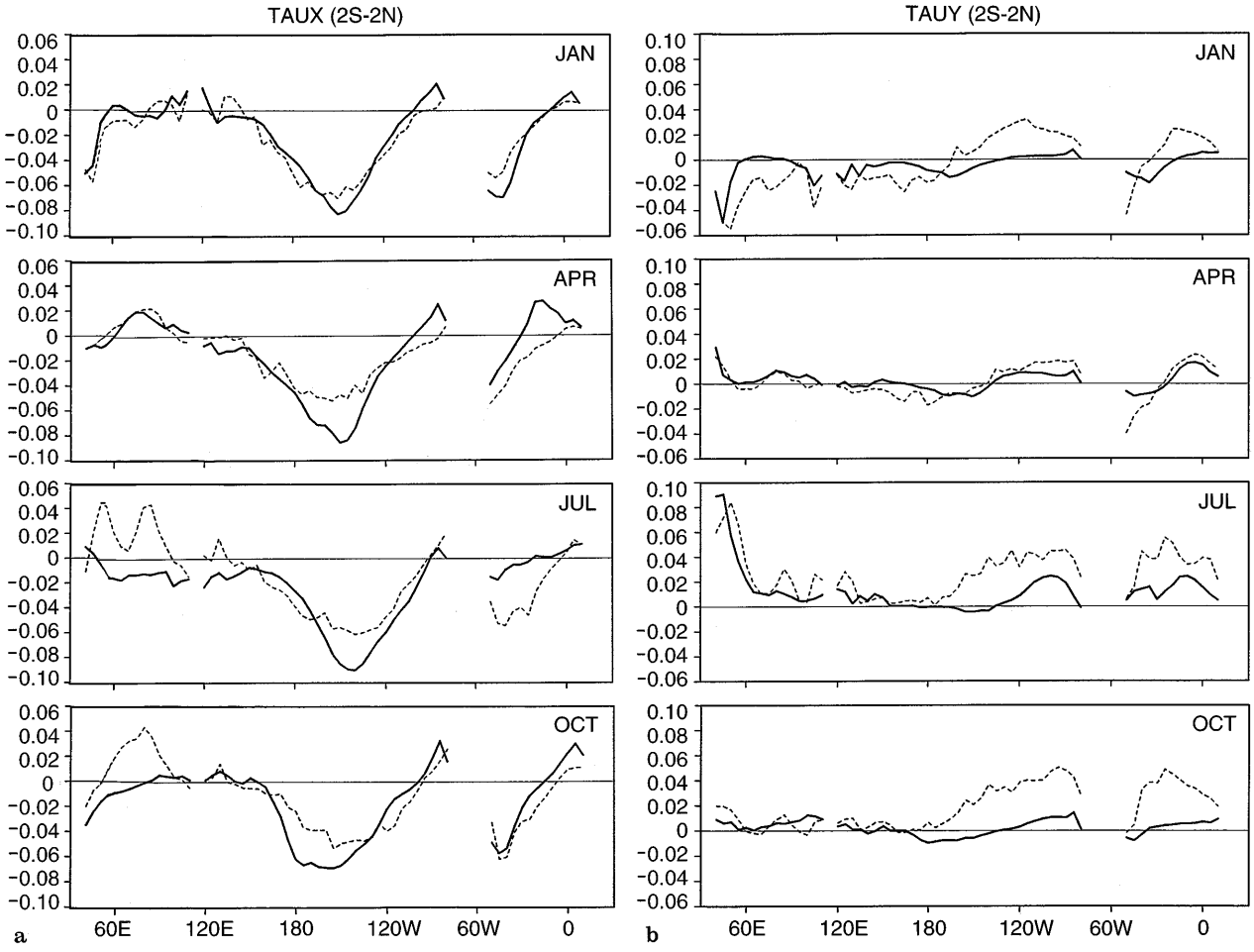

Fig. 3a, b. Seasonal variation of **a** zonal wind stress and **b** meridional wind stress along the equator (average between 2S and 2N) for the model climatology (*solid line*) and the observed climatology (Hellermann and Rosenstein 1983) multiplied by 0.75 (*dashed line*), respectively

Figure 4 shows the vertical cross section of annual mean temperature along the equator for the model and for the observation (Levitus 1982). The model succeeded in representing the Pacific equatorial thermocline structure. Over most of the Pacific sector, the model simulates the depth of the 20 °C isotherm with good agreement with the observations. At the eastern coast, however, the 20 °C isotherm declines toward east, which is not seen in the observations. This is probably caused by weak upwelling due to the unrealistic westerly wind stress along the eastern coast (Fig. 3a) and weak advection of cold water due to weak southerly wind stress along the west coast of South America (Fig. 3b). At all longitudes, the model thermocline is diffuse compared to that of observation. The model fails to reproduce the zonal gradient of the thermocline in the Indian ocean. This is related to differences in the wind direction at the equator, associated with variations in the southward extent of the westerly Indian summer monsoon between the model and the observations.

The structure of the subsurface basin-scale gyre is mainly controlled by the vorticity input of the large-scale wind stress. Figure 5 depicts the climatology of the annual mean ocean temperature of the subsurface (275 m depth) for (Fig. 5a) the model and (Fig. 5b) the observation (Levitus 1982). An overall pattern of the principal subtropical gyres is reproduced in the model. It is recognized that the model shows a weaker temperature gradient in the strong current regions compared with the observed field. Since horizontal resolution (2.5° × 2°) is not enough, the model simulates the Kuroshio transport only 38 Sv ($\times 10^6$ m^3/s) at maximum. The Kuroshio Extension is shifted north (around 40 °N). The subpolar gyre of the northern North Pacific is not sufficiently reproduced in the model.

4 Model ENSO

In this section, we overview ENSO-like variabilities in the equatorial Pacific reproduced in the model.

Figure 6, a, b shows time series of the simulated SST monthly anomaly at the equatorial central Pacific region (160 °E–160 °W, 6 °S–6 °N) and sea level pressure difference between Tahiti and Darwin, namely the

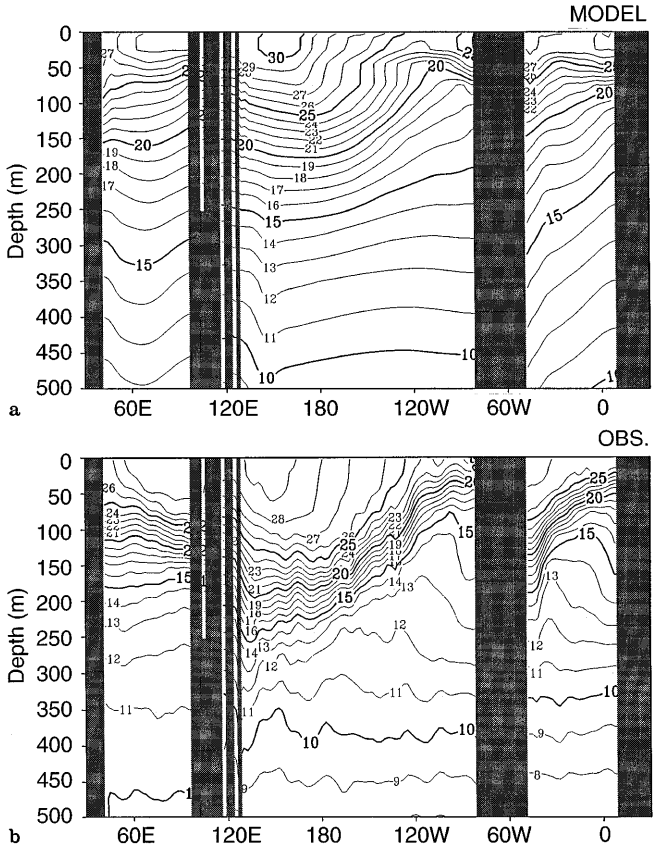

Fig. 4a, b. Longitude-depth cross section of the annual mean ocean temperature along the equator for **a** the model climatology and **b** the observed climatology (Levitus 1982). Contour interval is 1 °C

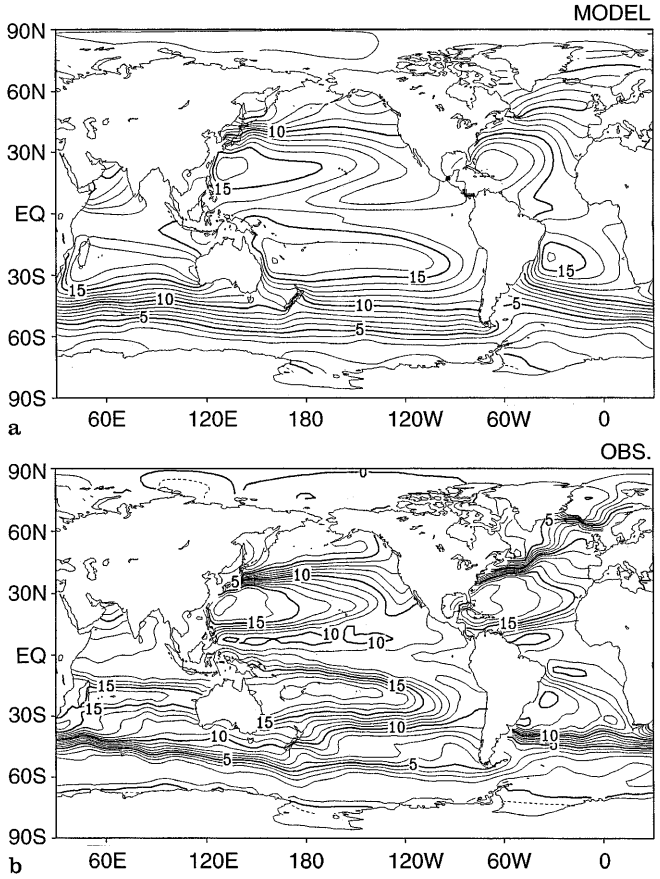

Fig. 5a, b. Annual mean ocean temperature at 275 m depth for **a** the model climatology and **b** the observed climatology (Levitus 1982). Contour interval is 1 °C

southern oscillation index (SOI). The SST anomaly and SOI show significant interannual oscillations with dominant periods of 3 to 6 years. The magnitude of the SST anomaly is about twice as large as that of previous coupled models (Philander et al. 1992; Nagai et al. 1992; Latif et al. 1993), though it is still small compared to the observed peak value of 3 °C. Our model has maximum variability of the SST around the date line, while it has smaller amplitude in the NINO3 region (150 °W–90 °W, 5 °S–5 °N) of the east-central Pacific (peak value 0.9 °C). This is due to a westward shift of the strongest zonal gradient of the equatorial SST in the model climatology. Time series of the model SOI also show an interannual variation which has negative correlation ($r-0.72$) with the SST anomaly. This correlation is comparable with that for the observed ENSO.

There are prominent 10 warm events and 8 cold events during the 70 y model integration. Common features of these events are typically seen in a warm event in the tenth year of the integration.

Figure 7a–d shows the time-longitude plots of anomalies for SST, zonal wind stress, vertical averaged temperature (VAT) along the equator, and VAT along 8 °N respectively. These variables are plotted for the years 9 to 13. VAT represents the ocean heat content of the upper 300 m of ocean.

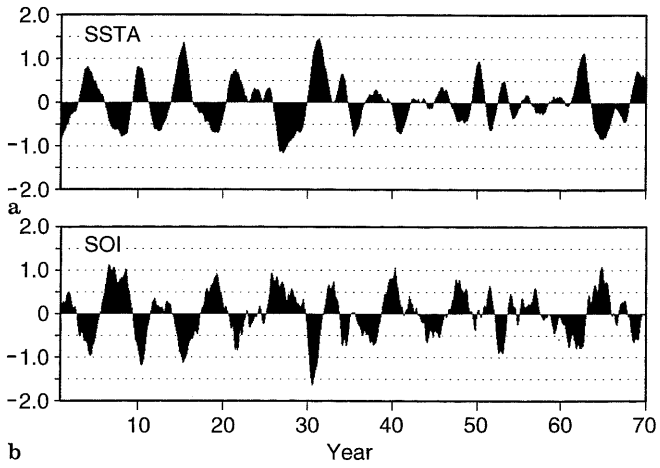

Fig. 6a, b. Time series of simulated **a** SST anomaly in the central equatorial Pacific region (160 °E–160 °W, 6S–6N) and **b** SOI, for the 70 y model run. *Values* are 13 month running means

Preceding the warm event, VAT along the equator increases in the western Pacific and decreases at the east-central Pacific. This is equivalent to a deepening of the thermocline at the western boundary and a shoaling at the east-central Pacific. During this period,

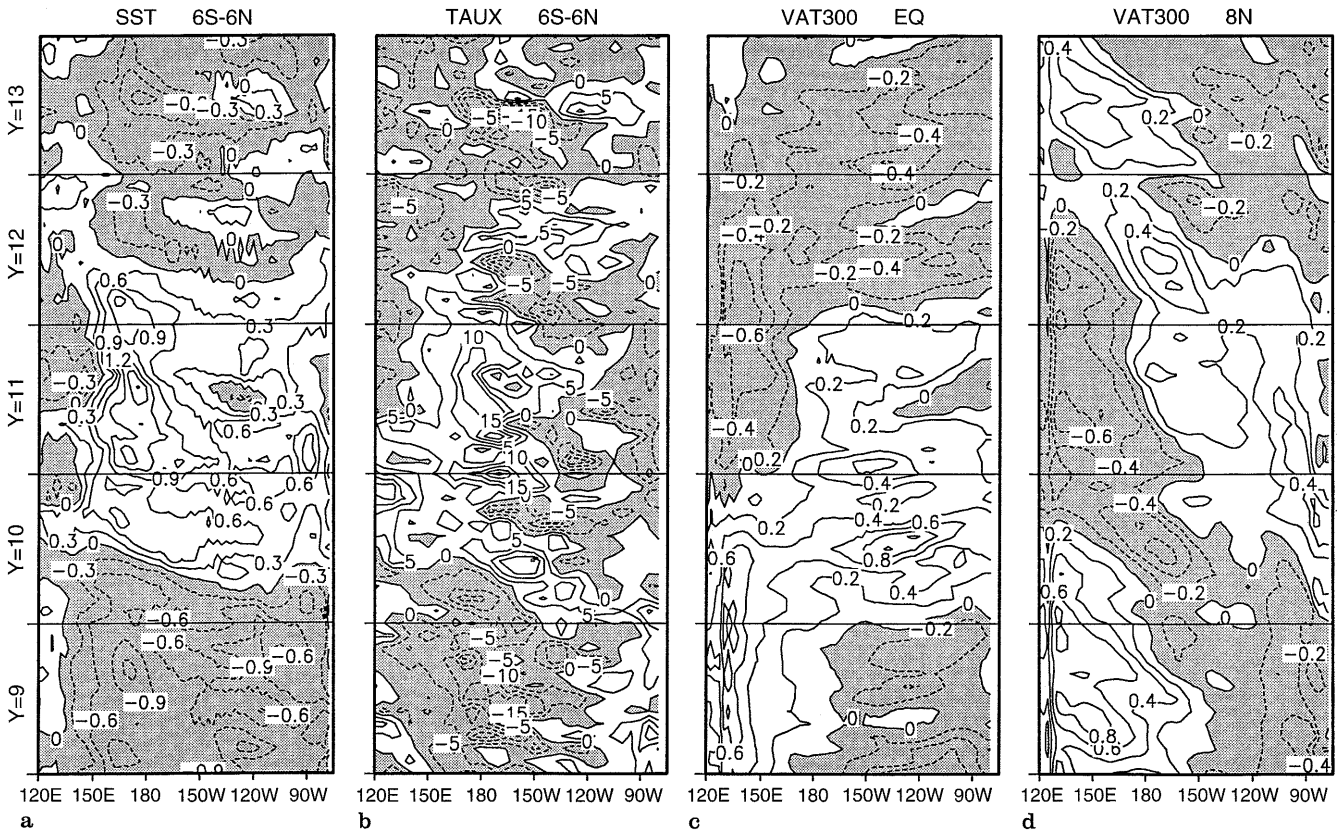

Fig. 7a–d. Longitude-time plot for anomalies of **a** SST (average between 6°S and 6°N), **b** zonal wind stress (average between 6°S and 6°N), **c** VAT along the equator and **d** VAT along 8°N. Time covers years 9 to 13 of the model run. *Negative* values are *shaded.* Contour intervals are **a** 0.3 °C, **b** 0.05 N/m^2, **c** 0.2 °C and **d** 0.2 °C

a large easterly wind anomaly in the central Pacific is sustained. The VAT positive anomaly in the equatorial western boundary begins to propagate eastward in January of year 10, and reaches the eastern boundary in March of year 10 (Fig. 7c). It takes about 2–3 months for the signal to cross the basin. The propagation speed is comparable with that of the first equatorial Kelvin mode. The beginning of the signal propagation is seasonally phase-locked to boreal winter in most of the model events. It can be seen that several pulses of VAT anomalies (which follow impulsive westerly wind anomalies in the central Pacific) propagate successively for more than one year, and subsequently, the positive VAT anomaly in the western Pacific disappears.

Warming of the SST starts at the east-central Pacific when the first VAT anomaly arrives at the eastern Pacific. The SST warming which is initiated at the eastern Pacific extends westward accompanying the westerly wind stress anomaly (Fig. 7a, b). In the mature stage of the model warm event, SST warming is enhanced around the date line, and a westerly wind stress anomaly becomes dominant in the central Pacific. To the west of the date line, at the mature stage of the SST warming, a significant positive downward heat flux anomaly at the ocean surface (not shown here) corresponds with the SST warming.

It is clearly seen that westerly wind stress anomalies in the central equatorial Pacific generate negative VAT signals away from the equator (Fig. 7d) by weakening of the Ekman convergence there. These negative VAT signals propagate westward and reach the western boundary. It takes about 6 months for the signals to cross half of the basin. Its propagation speed approximately corresponds to the group velocity of an oceanic Rossby wave along this latitude. The propagation of this off-equatrial signal contributes to the decrease of ocean heat content in the western Pacific. After the decrease of ocean heat content in the western Pacific, a negative signal propagates eastward, in turn (at the beginning of year 12). Variations similar to these mentioned with the opposite sign are repeated as the next La Niña phase. This cycle in the model ENSO is similar to the delayed-oscillator discussed by Schopf and Suarez (1988) and Nagai et al. (1992).

5 Interannual variabilities in mid-high latitudes

The power spectra of the SST is estimated to determine dominant time scales in the whole Pacific region. Figure 8 shows power spectra of the model SST averaged over the Indo-Pacific region (region A: 30°E–60°W, 40°S–50°N), the central equatorial Pacific region (region B: 160°E–160°W, 6°S–6°N) and the central North Pacific region (region C: 160°E–160°W, 30°N–42°N). There are peaks at periods around 4 y, 6 y, 8–9 y and 20–30 y for all the regions. Since a dis-

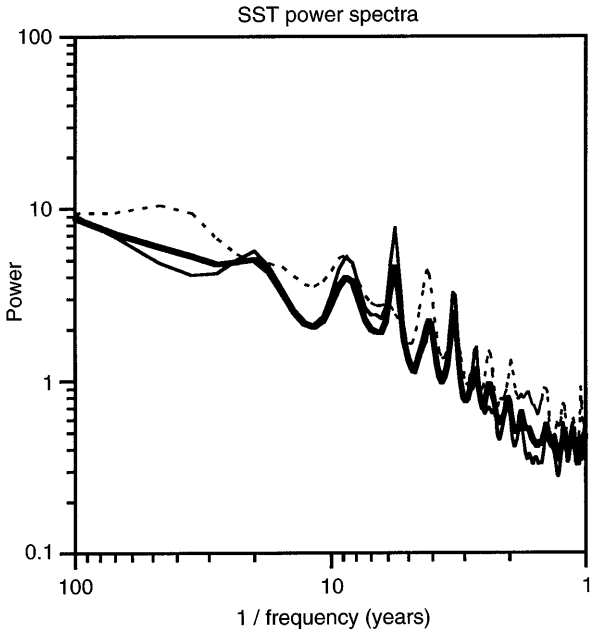

Fig. 8. Area-averaged power spectral density of the simulated SST. *Bold line, thin line* and *dashed line* indicate averages for the Indo-Pacific region (30°E–60°W, 4°S–50°N), the central equatorial Pacific region (160°E–160°W, 6°S–6°N) and the central North Pacific region (160°E–160°W, 30°N–42°N), respectively. Linear trends of SSTs are removed for each grid point before calculating spectra

tinct gap in the spectra is recognized at the 12 y period, we define (1) variation with the 2 to 12 y period as an ENSO time scale variation and (2) variation where the period is longer than 12 y as an interdecadal time scale variation. We separated these variations by applying time filters for the annual mean data set. Then, empirical orthogonal function (EOF) analyses were made for those time filtered data of the Indo-Pacific region (region A). Calculation of the EOFs are based on a variance-covariance matrix in order to work out the relative magnitude of the variations. In this section, we focus on the ENSO time scale variation of the Pacific in the mid-high latitudes.

Figure 9 shows EOFs of the first mode (EOF1) for the ENSO time scale variation of the simulated SST and wind stress. The EOF1 of the SST and the wind stress accounts for 30.8% and 20.4% of all variance in this time scale, respectively. The spatial pattern of the EOF1 of SST indicates that there is an intensive positive signal in the central equatorial Pacific where the model ENSO shows maximum SST variations. Notable peaks in the temporal coefficients coincide with years of the prominent events in the model ENSO (Fig. 6). Accordingly, it is considered that this EOF1 mode represents variations in the equatorial Pacific region associated with the model ENSO. In the mid-high latitudes, the EOF1 of SST shows as positive in the eastern Pacific, especially between Hawaii and off California and as negative in the central North Pacific and the west-central South Pacific. This wedge shaped pattern is also typically seen in the EOF1 of the observed SST in the same time scale (see Fig. 15a).

The EOF1 of the wind stress also corresponds to the variation associated with the model ENSO, since the temporal coefficients correlates well with that of the EOF1 of the SST ($r=0.82$). During the maximum phase of the equatorial SST, a large westerly wind stress anomaly in the western equatorial Pacific and the convergence of anomalous wind stress from the equator (around 150°W) to 120°W–12°S in the South Pacific, are clearly seen. This feature of the wind stress anomaly is well documented in the observed El Niño

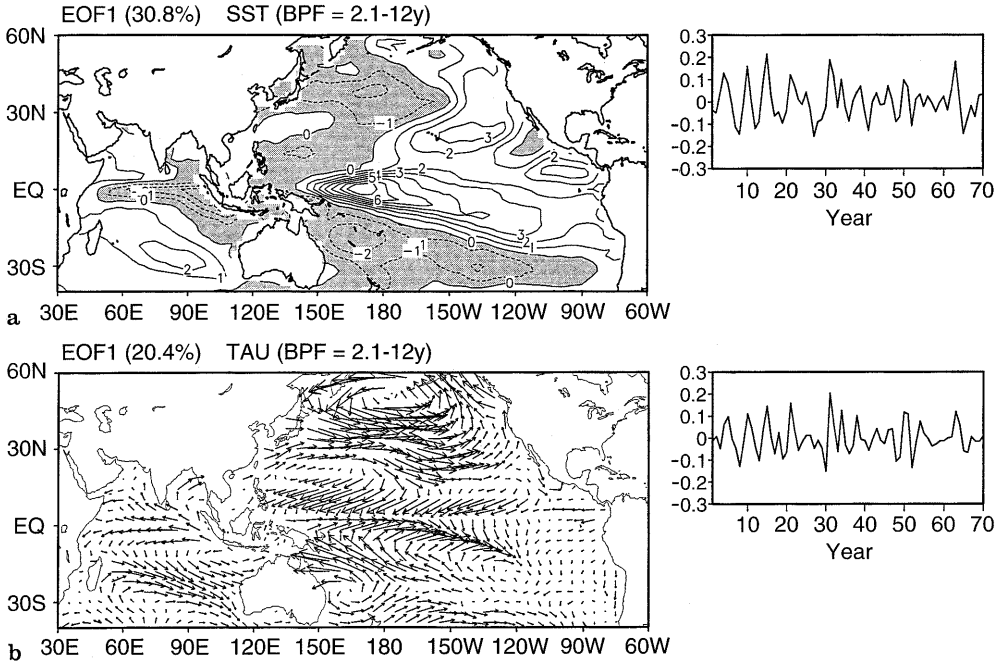

Fig. 9a, b. Eigenvectors and time coefficients of the first EOFs of simulated **a** SST and **b** wind stress for ENSO time scale (2–12 y). *Negative* region is *shaded* in **a**. Values of eigenvectors are in proportion to amplitude of variance, since EOFs are calculated for variance matrix

(e.g., Rasmusson and Carpenter 1982). In the central North Pacific, there is a dominant westerly wind anomaly and a cyclonic wind anomaly on its northern side which corresponds to the intensification of the Aleutian low in winter. The eastern North Pacific around Hawaii is also dominated by the westerly wind stress anomaly (Fig. 9b). This results in weakened northeast trade winds and a suppression of evaporation which contribute to warming of the SST there. Along the coast of Canada and Alaska, a strong southerly wind anomaly, which leads warm air advection, is expected to raise the SST there as is seen in the EOF1 of SST (Fig. 9a). An associated variation is also recognized in the 500 hPa geopotential height (Z500). The correlation map between Z500 of northern winter (December to February) and the time coefficient of the EOF1 of the SST for the ENSO time scale (Fig. 10a) shows the largest positive correlation in the tropical Pacific and marked negative correlation in the North Pacific with a center at around 170°E, 45°N. Another positive correlation is seen in North America centered over the western part of Canada. These features are seen in similar correlation map for the observations (Fig. 10b). These PNA-like teleconnections originate from the equatorial Pacific as a midlatitude atmospheric response of the Northern Hemisphere to the warm SST anomaly in the tropics (Horel and Wallace 1981).

In order to see whether the SST anomaly is forced by the surface heat flux, or the surface heat flux is controlled by the SST, for the ENSO time scale, we examine correlation between temporal coefficient of the EOF1 of the SST and total heat flux (including radiative flux) at the ocean surface (Fig. 11a). Apart from the equatorial region, the heat flux anomaly is positive downward where the SST anomaly is positive, and vice versa. It implies that the extratropical SST is forced by the surface heat flux variation at the ENSO time scales. In order to see whether the surface heat flux anomaly is a dominant factor of the extratropical SST change in terms of heat budget, correlation between the SST tendency anomaly and the surface heat flux anomaly for the northern winter (December to February) is examined (Fig. 11b). The seasonal mean SST tendency is defined from the raw monthly mean data. It is found that the correlation is higher than 0.6 in a large part of the midlatitudes of the Pacific. The area averaged correlation is 0.78 for the central North Pacific (160°E–160°W, 30°N–42°N) and 0.91 for the region east of Hawaii (160°W–120°W, 14°N–26°N), where large values appeared in the spatial EOF1 of SST (Fig. 9a). Correlation of the midlatitudes in summer (not shown here) has qualitatively similar features to those in winter, and has slightly smaller value. Although the correlation north of 40°N in winter is low (Fig. 11b), the correlation north of 40°N in summer is close to that in the midlatitudes. Analysis of SST heat budget shows that the heat flux anomaly accounts for large part of the SST tendency anomaly in the midlatituding North Pacific. The SST variation in these regions is, therefore, mainly controlled by the surface heat flux variation at the ENSO time scale.

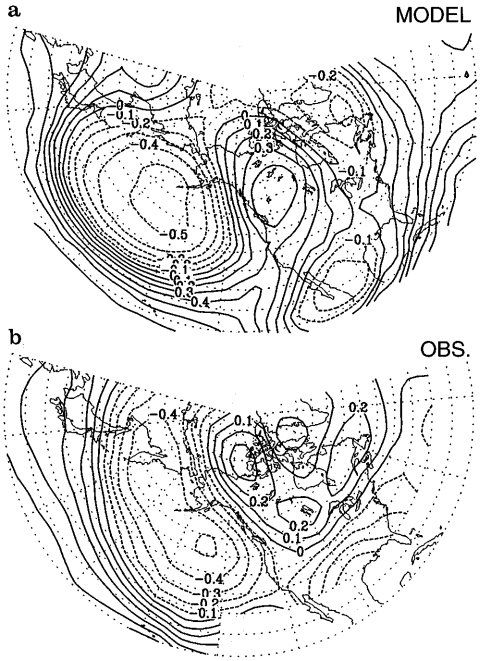

Fig. 10a, b. Correlation between boreal winter (December to February) Z500 and temporal coefficient of EOF1 of the SST for the ENSO time scale, for **a** the model and **b** the observations, respectively. Observed correlations are calculated for the period 1946–1992

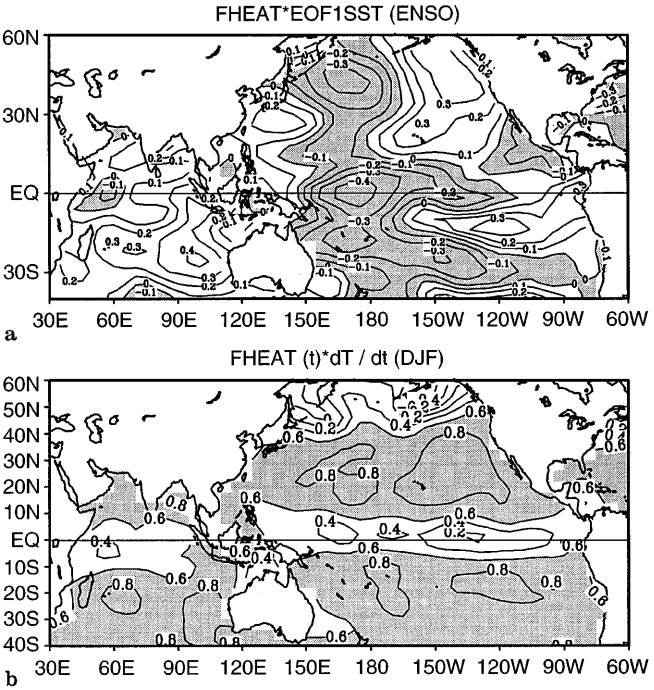

Fig. 11. a Correlation between downward heat flux (sensible + latent heat and net radiative flux) at the ocean surface and temporal coefficient of the first EOF of the SST for the ENSO time scale. *Negative* regions are *shaded.* **b** Correlation between the SST tendency anomaly and the downward surface heat flux anomaly for the northern winter (December to January). The SST tendency is defined from the raw monthly mean data. *High correlation* ($r > 0.6$) regions are shaded

Ocean subsurface variation in the whole Pacific in relation with the model ENSO is examined. The vertical averaged temperature (VAT) over the upper 300 m of the ocean is used as an indicator of the ocean subsurface variation, and the temporal coefficient of EOF1 of the SST for the ENSO time scale is chosen as an indicator of the model ENSO. Figure 12 shows lagged regressions of the VAT from the temporal coefficient of EOF1 of the SST.

In the tropical Pacific, VAT variation associated with the ENSO is apparent. Preceding the maximum phase of the model ENSO (lag = −1: Fig. 12a) a positive equatorial signal suggesting a propagation of an equatorial Kelvin wave is notable. In the following 2 years, it appears that a negative signal off the equator propagates westward and reaches the western boundary (Fig. 12b–c).

In the midlatitudes of the North Pacific, significant variation is found to be associated with the model ENSO. Negative anomalies appear in the central North Pacific (A in Fig. 12b) and the Kuroshio extension region (B in Fig. 12b) at the maximum phase of the model ENSO. The negative anomalies (A and B) develop and are combined one year later (C in Fig. 12c). Afterwards, the southern portion of the developed anomaly (C) migrates westward and reaches the western Pacific (Fig. 12d–e). A similar signal with the opposite sign to signal A is seen where lag = 3 years (D in Fig. 12e), which has migrated from offshore of California. Propagation of these signals and their enhancement in the central North Pacific are evident in the vertical zonal cross section along 32°N for similar lag regression analyses (Fig. 13a–e). It has been analyzed to show that horizontal pattern of the shallow signals is consistent with heating and cooling region shown in Fig. 10a. A warming in the eastern part and a cooling in the central part of the surface layer (~100 m) are separated from the deeper signals in the subsurface (Fig. 13a, b). Westward propagation of the subsurface signals (200 m ~ 500 m depth) is clearly seen: for example, a negative signal around 150°W at lag = −1 year migrates to 160°E during the following 4 years. The propagation speed (~5 cm/s) is almost comparable to the group velocity of oceanic first baroclinic Rossby wave at this latitude in the model.

After a year beyond the maximum phase (lag = 1), cooling in the central Pacific extends beyond 800 m depth (Fig. 13b, c). Location of the negative subsurface signal around 160°W corresponds to that of the large positive vorticity of the wind stress anomaly (Fig. 9b). It is considered, therefore, that the development of this subsurface signal is a dynamical response to the wind forcing through the Ekman pumping.

6 Interdecadal variabilities in the Pacific

The power spectra of the SST in the Pacific (Fig. 8) indicates decadal to interdecadal variations as well as the ENSO time scale variation as mentioned by Tokioka et al. (1995). In this section we show structure of the interdecadal variation in the Pacific with analyses of the low-pass filtered data (the cut-off period is 12 y).

Figure 14 shows the EOF1 for the interdecadal variations of SST and wind stress. The EOF1 for the SST and the wind stress accounts for 36.4% and 38.8% of all the variance for this time scale, respectively. The spatial EOF1 for the interdecadal SST variation reveals a marked negative correlation of the central North Pacific with the tropical SST. It shows a similar geographical pattern with that for the ENSO time scale (see Fig. 9a). The interdecadal variation of SST, however, has a larger amplitude in the central North Pacific relative to that over the equator, however, for the ENSO time scale, the equatorial amplitude is much larger than that of the North Pacific. It is noteworthy that this feature is also found in similar EOF analyses for the observed SST (Fig. 15). For the EOF1 of the observed SST, both the ENSO time scale and the interdecadal time scale show a wedge-shaped pattern with its apex at the central equatorial Pacific. It is easy to see the difference in relative amplitudes of the SST anomalies in the tropics to those in the extratropics between the interdecadal time scale (Fig. 15b) and the ENSO time scale (Fig. 15a). The temporal coefficient for the model SST may be contaminated by climatic drift due to residual spin-up of the model. It should also be noted that period of the observed SST data is not long enough to determine statistically whether it represents a trend or oscillations. The spatial patterns, however, strongly suggest a robust relationship for the model and the observations.

An EOF1 for the wind stress variation of the interdecadal time scale (Fig. 14b) shows a similar general spatial pattern with that for the model ENSO time scale (Fig. 9b). There is a westerly anomaly in the west-central equatorial Pacific and a cyclonic anomaly in the central North Pacific associated with an intensification of the Aleutian Low. The correlation map of Z500 with EOF1 of the SST for the interdecadal time scale (not shown) also indicates a PNA-like pattern similar to that for the ENSO time scale (Fig. 11a). Some differences are seen between the two time scales. For the interdecadal time scale, the magnitude of the wind stress anomaly in the midlatitude is as large as in the equatorial west-central region. For the ENSO time scale, on the other hand, the wind stress anomaly in the central North Pacific is larger than that in the tropics. It is also noted that the axis of the maximum anomalous westerly wind in the central North Pacific slightly shifts to the north for the interdecadal time scale (~45°N) compared to that for the ENSO time scale (~40°N).

Difference of variances between the ENSO and the interdecadal time scales can be found by comparing Fig. 9 and Fig. 14 directly, since the loading factors of spatial EOFs are plotted with the same unit of variances. Relationship of relative magnitudes of variations of SST and wind stress for the tropics versus the extratropics between the ENSO and the interdecadal time scales is summarized in Table 1. In the central North Pacific, it is found that the interdecadal SST var-

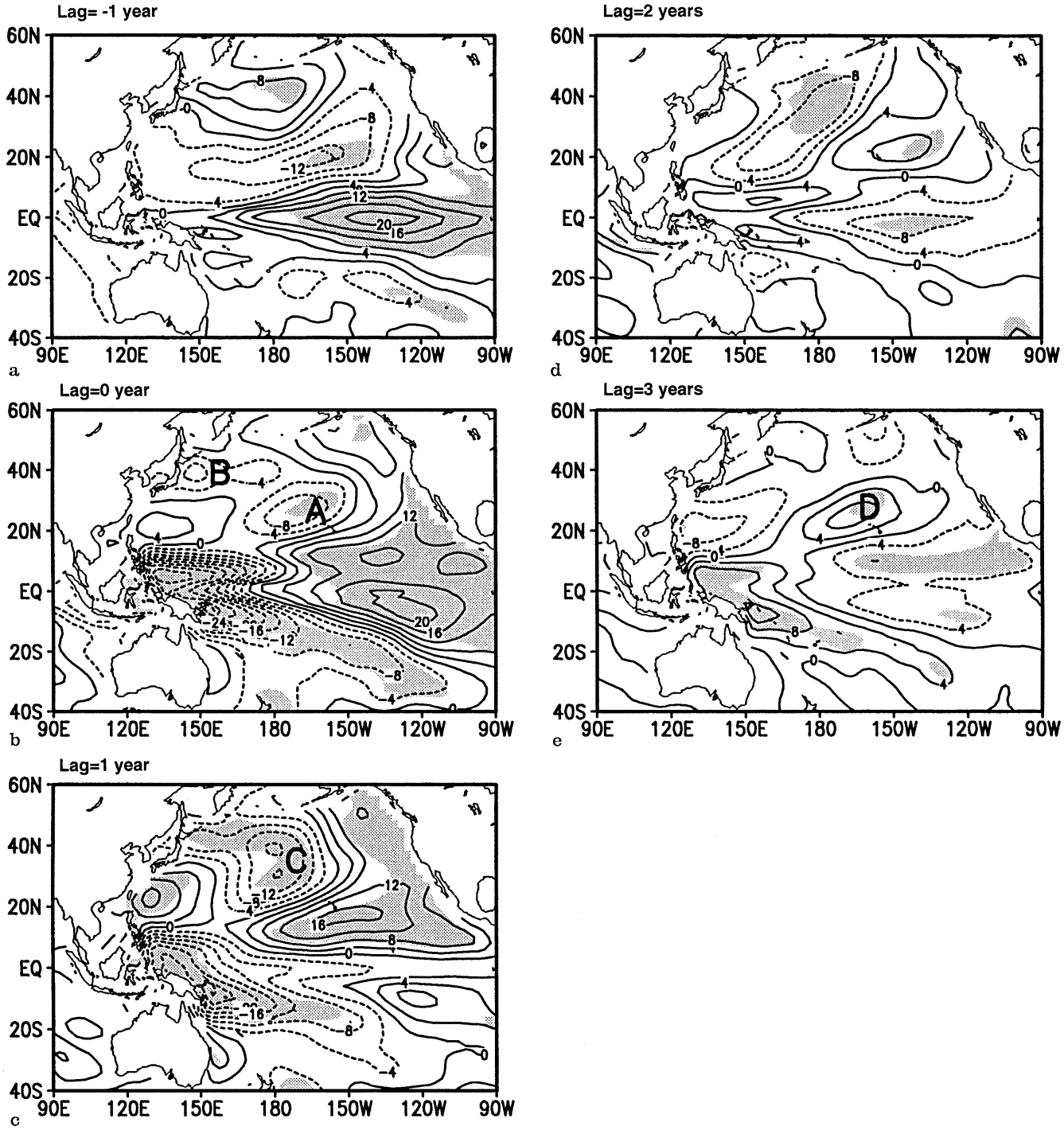

Fig. 12a–e. Lag-regressions of VAT with time coefficient of EOF1 of the SST for the ENSO time scale. **a** lag = −1 year, **b** lag = 0, **c** lag = 1 year, **d** lag = 2 years, **e** lag = 3 years. *High correlation* ($|r| > 0.4$) is shown in *shaded* region. Units are relative

Table 1. Relationship of relative magnitudes of variations of SST and wind stress for the tropics versus the extratropics. D and E denote magnitude of variation for the interdecadal time scale and the ENSO time scale, respectively

	SST variation	Wind variation
Midlatitude	D > E	D < E
Tropics	D < E	D ~ E

iation is larger than the ENSO time scale SST variation, and the interdecadal wind variation is smaller than ENSO time scale wind variation. In the equatorial Pacific, on the other hand, the ENSO time scale SST variation is larger than interdecadal SST variation, and the interdecadal wind variation is as large as ENSO time scale wind variation.

We examined variations of the ocean subsurface in association with the wind stress variations for the inter-

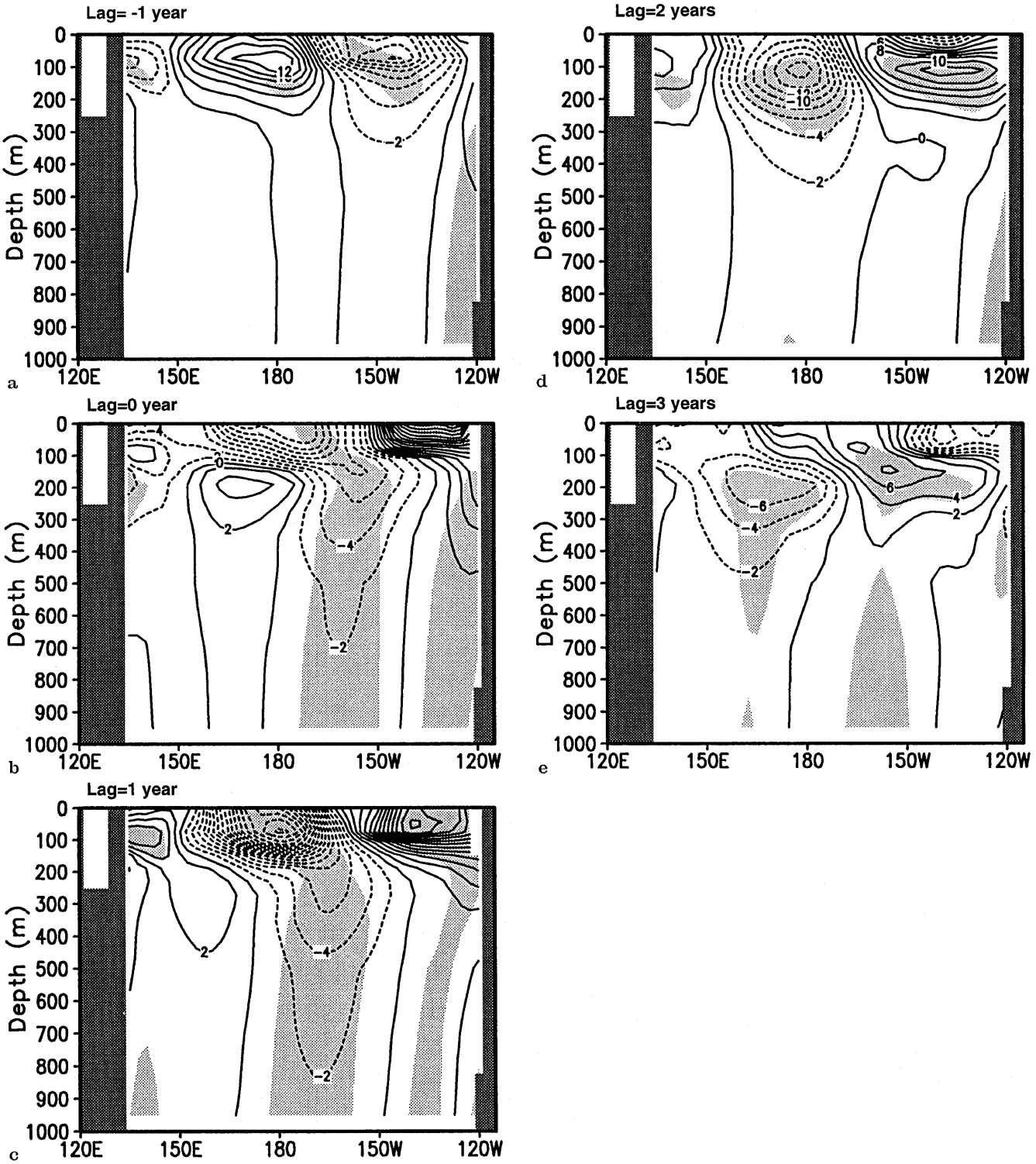

Fig. 13a–e. Lag-regressions of ocean temperature in zonal-vertical cross section along 32°N with time coefficient of the EOF1 of SST for the ENSO time scale. **a** lag = −1 year, **b** lag = 0, **c** lag = 1 year, **d** lag = 2 years, **e** lag = 3 years. Units are relative. *High correlation* ($|r| > 0.4$) regions are *shaded*

decadal time scale. The temporal coefficient of EOF1 of the wind stress for the interdecadal time scale is applied as an indicator of the interdecadal wind stress variation. Lagged regression of VAT from the temporal coefficient of EOF1 of the wind stress for the interdecadal time scale (Fig. 16a–d) shows that a negative anomaly in the central North Pacific slowly migrates westward. This variation is considered as spin-up of the ocean subtropical gyre in response to the wind stress variation in the midlatitude.

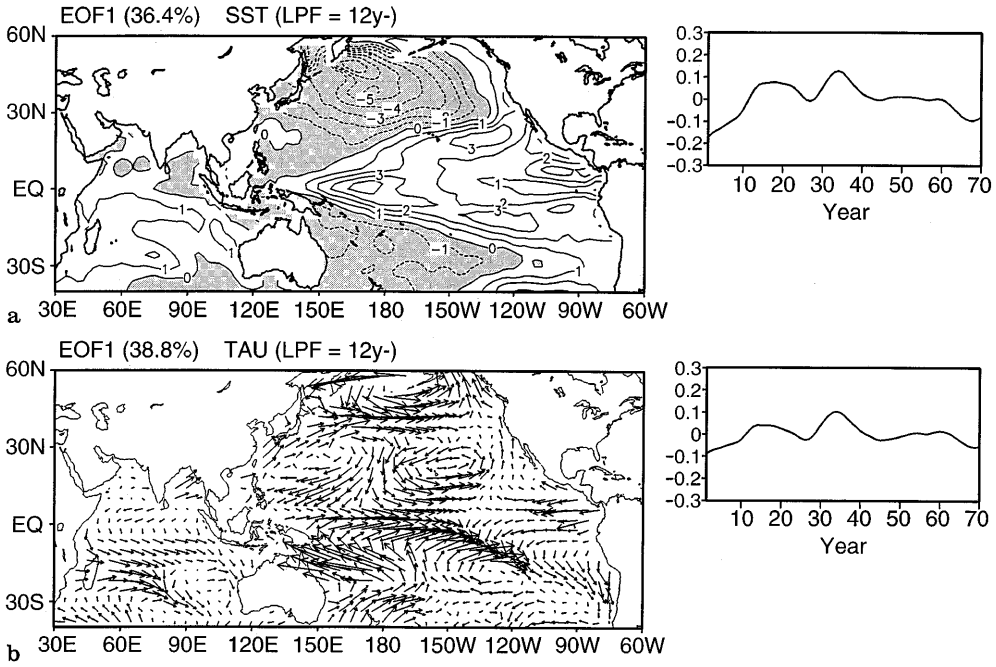

Fig. 14a, b. Same as Fig. 9 but for interdecadal time scale (periods longer than 12 y)

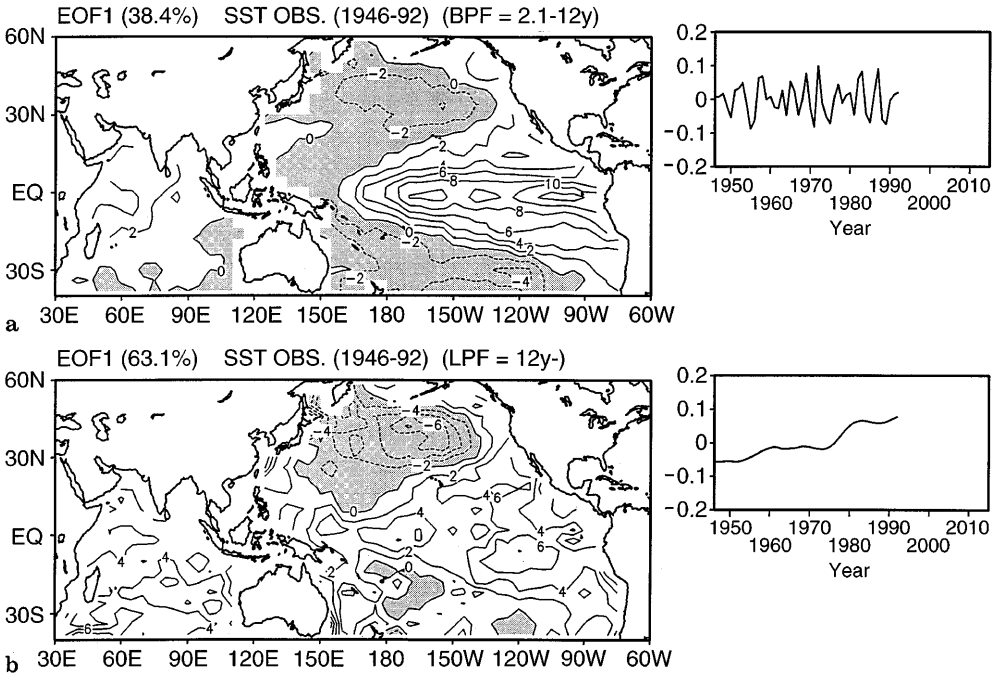

Fig. 15a, b. Eigenvectors of the first EOFs of the SST observed from 1946 to 1992, for **a** ENSO time scale and **b** interdecadal time scale. *Negative* region is *shaded.* Values of eigenvectors are in proportion to amplitude of variance, since EOFs are calculated for variance matrix

It is suggested that the surface heat flux and/or the Ekman heat transport also contribute to the VAT change, because its spatial pattern (Fig. 16a) has strong similarity with the SST pattern (see Fig. 14a) in the extratropics. More detailed analysis is required to estimate relative magnitudes of the individual contribution.

We notice that horizontal structure of the ocean subsurface variation in the tropical Pacific and the eastern Pacific of the midlatitudes resembles that of ENSO time scale in some phases. For example, geographical patterns in the tropical Pacific and the eastern Pacific of the midlatitude for lag = 0 year through lag = 4 years (Fig. 16a–c) are similar to those for lag = 0 through lag = 1 for the ENSO time scale (Fig. 12b–c). It is also seen that positive anomalies in the eastern North Pacific extend westward along the tropical latitudes between 10°N to 20°N, and reach the Western Pacific close to the Philippines at 10 years lag time. In addition, a negative signal near New Zealand at first (Fig. 16a) appears to migrate eastward until it reaches near to 140°W at 10 years lag time (Fig. 16f).

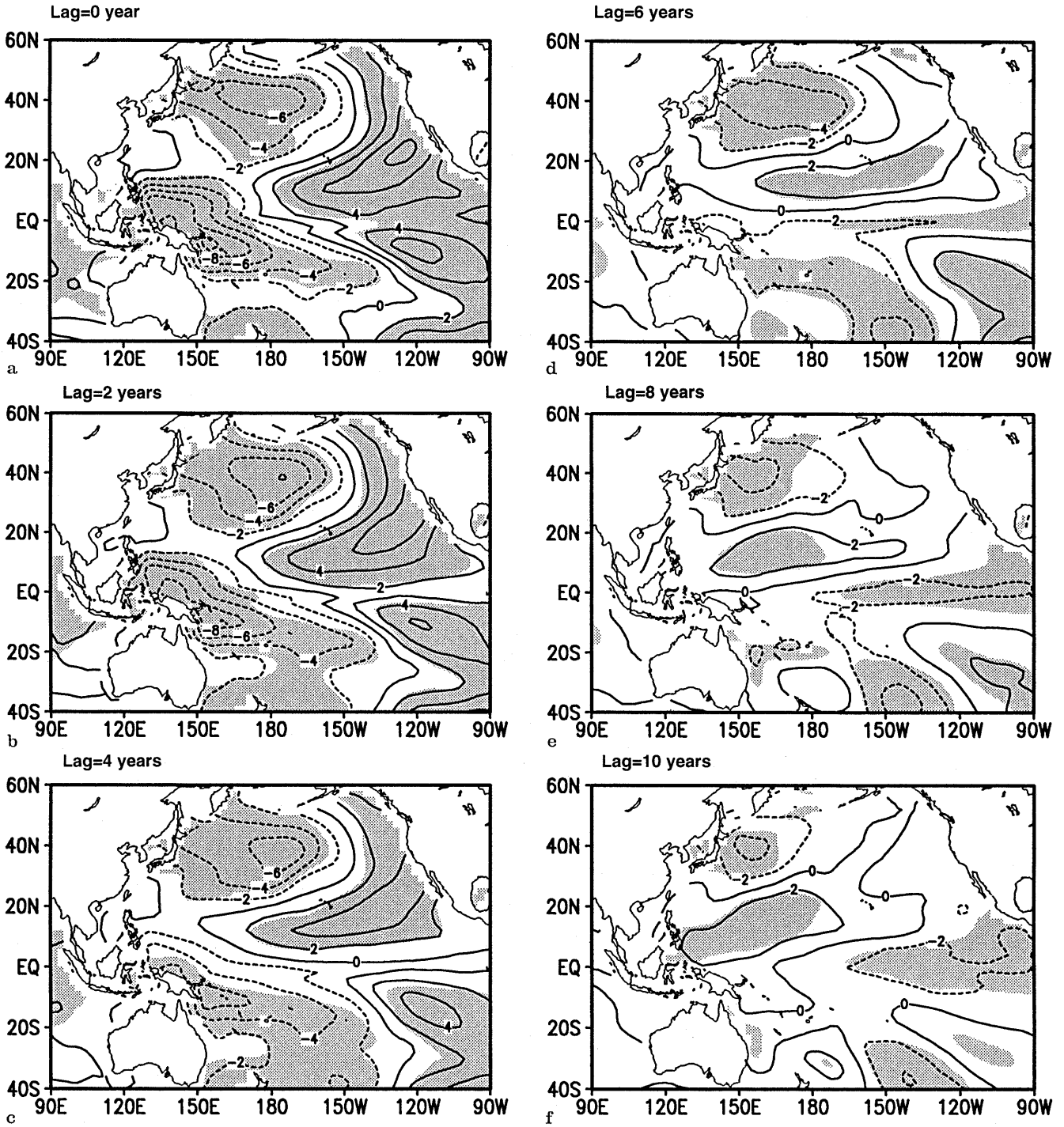

Fig. 16a–f. Lag-regressions of VAT with time coefficient of the EOF1 of the wind stress for the interdecadal time scale; **a** lag = 0, **b** lag = 2 years, **c** lag = 4 years, **d** lag = 6 years, **e** lag = 8 years, **f** lag = 10 years. Units are relative. *High* correlation ($|r| > 0.6$) regions are *shaded*

The Meridional structure of the interdecadal temperature variation along 175°E is shown in Fig. 17. It is apparent that there are subsurface signals (below ~100 m depth) independent of shallow signals which are confined to surface layer (surface to ~100 m depth). A negative anomaly, which extends deeper than 800 m at around 50°N, develops until 6 years lag time is reached (Fig. 17a–d). This cold signal corresponds to the negative VAT signal of the central North Pacific shown in Fig. 16. A positive anomaly intruded from the east along the 10°N–20°N latitudes at around the 200 m depth, becomes significant after 6 years lag time (Fig. 17d–f), with significant amplitude down to 1000 m depth. This warm signal is identical to the westward expansion of the positive VAT signal along 10°N–20°N shown in Fig. 16d–f. It is noticed that this

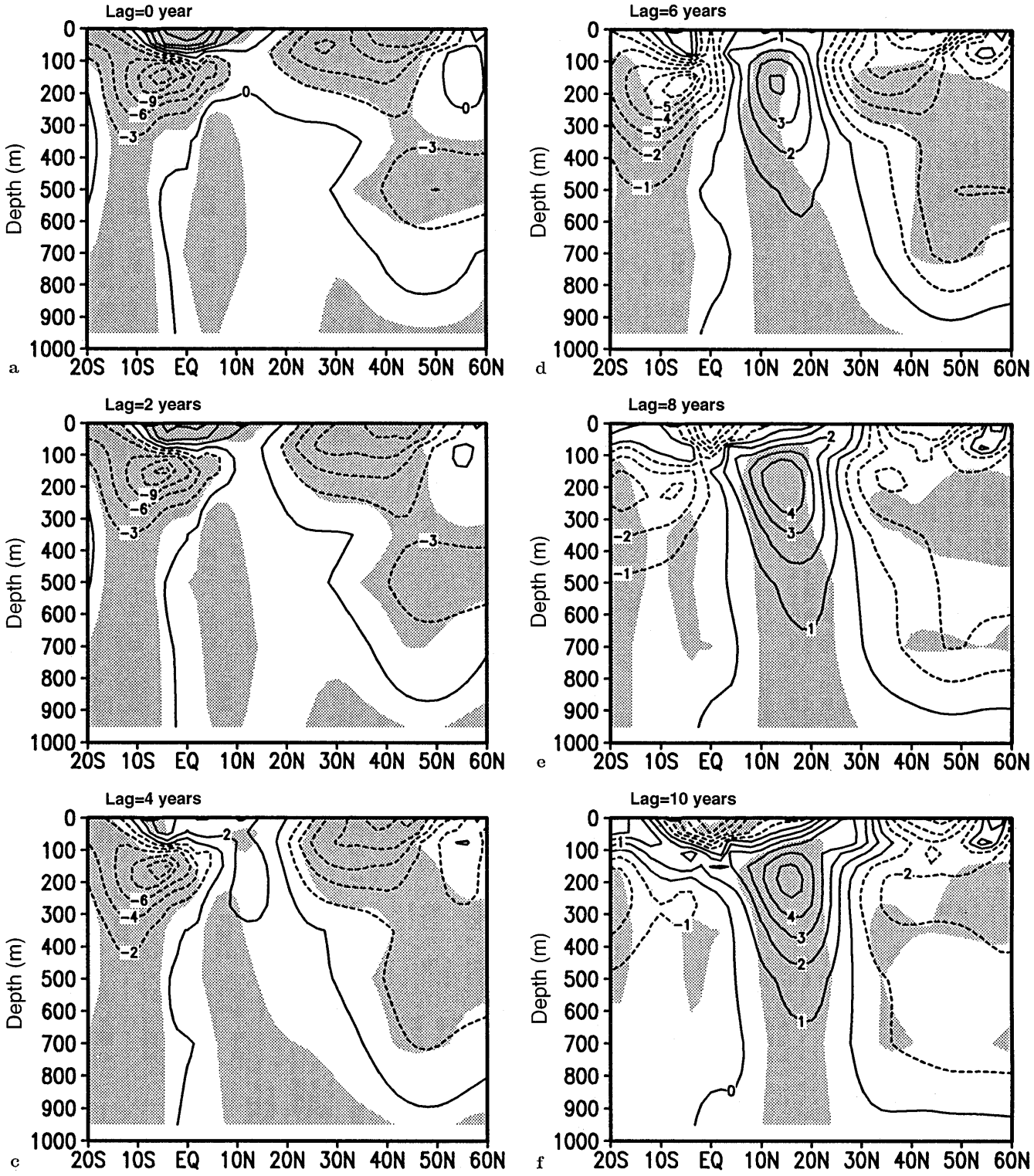

Fig. 17a–f. Lag-regressions of ocean temperature in meridional-vertical cross section along 175°E with time coefficient of the EOF1 of the wind stress for the interdecadal time scale; **a** lag = 0, **b** lag = 2 years, **c** lag = 4 years, **d** lag = 6 years, **e** lag = 8 years, **f** lag = 10 years. Units are relative. *High correlation* ($|r| > 0.6$) regions are *shaded*

meridional structure in the subsurface is symmetrical to the 15°N–20°N latitude, though the horizontal structure of the SST variation seems symmetrical to the equator (Fig. 14a). Watanabe and Mizuno (1995) reported the vertical structure of the observed temperature difference along the 170°E–180°E longitude band between 1966–75 and 1976–85 (Fig. 3 of Watanabe and Mizuno 1995). It is remarkable that this meridional-vertical structure in Fig. 17d is quite similar to that of the interdecadal change observed in the mid 1970s.

7 Summary and discussion

Interannual and interdecadal time scale variations in the Pacific region are investigated with the analysis of a 70 y integration of a coupled atmosphere-ocean GCM developed at MRI. The climatology of the annual mean state and seasonal variation are realistically reproduced by the model.

The model reveals interannual variability in the tropical Pacific which has several typical characteristics of the observed ENSO. The oceanic heat, which is piled up in the equatorial western Pacific preceding the warm event, propagates eastward as an equatorial Kelvin wave and brings about the warming of the SST in the eastern Pacific. In the model events, however, there is no indication of eastward evolution of SST and wind stress coupled with Kelvin wave propagation (Philander et al. 1984). The SST warming spreads westward, accompanied by the westward propagation of the westerly wind stress anomaly. This stage reminds us of an SST mode (Neelin 1991) which behaves as a wind stress-upwelling feedback. Similar behavior of SST signals with global coupled models were reported by Meehl (1990) and Lau et al. (1992). At the mature stage, the SST warming develops around the date line with increased downward surface heat flux. The model shows that westward propagation of the oceanic heat content off the equator contributes to the pile-up of ocean heat content in the western Pacific to prepare the next event. This cycle implies the delayed-oscillator mechanism of the model ENSO.

Both for the ENSO and the interdecadal time scales, variations of SST, atmospheric circulation and ocean subsurface show coherent spatial structures in the whole Pacific. The spatial structure of the variation in the model corresponds well to the observed one.

Basin-scale features of the principal SST variation for the ENSO time scale (representing the model ENSO in the tropics) show negative correlation in the central North Pacific with tropical SST, and are similar to that of the observed one. The associated variation of the atmosphere indicates the intensification of the Aleutian Low and the PNA-like teleconnection pattern as a response to the tropical warm SST anomaly. It is shown that the surface heat flux associated with atmospheric circulation changes is a dominant factor for the midlatitude SST variation in the North Pacific. Tokioka et al. (1993) argued that the enhanced Aleutian Low in winter contributes to cooling in the central North Pacific ocean by increase of evaporation and southward cold water advection by the Ekman transport in a coupled GCM. Miller (1992) also reported the similar result with a simple coupled model. Our result is consistent with those studies.

It is shown that the ENSO time scale variability of the midlatitude ocean consists of the westward propagation of the subsurface temperature signal and the temperature variation within the shallow mixed layer forced by atmospheric heat fluxes. Let us discuss the temporal evolution of the negative subsurface temperature anomaly. The negative anomaly is apparently either originated by the last La Niña along the eastern coast of the North Pacific, or generated by the northerly wind anomaly along the Californian coast. This negative anomaly migrates westward as an oceanic Rossby wave, while the next El Niño occurs. Figure 13 shows that wind forcing, as a result of atmospheric response to the El Niño, contributes to enhancing this signal through both surface cooling and positive vorticity input. Consequently, the negative anomaly is enhanced sufficiently to sustain its amplitude until it reaches the western Pacific. Thus, close time scales of the model ENSO and the westward propagation of the midlatitude subsurface signal across the basin may enhance midlatitude oceanic variation in the ENSO time scale.

Compared with the ENSO time scale, SST variation for the interdecadal time scale shows similar geographical patterns of positive/negative area, but has a larger relative amplitude in the central North Pacific than that in the tropics. For the atmosphere, spatial structures of the variations in the two time scales are similar to each other.

Based on Table 1, we consider that the interdecadal variation of the extratropical atmospheric circulation is forced mainly by the interdecadal tropical SST variation. Since the variation of equatorial SST is relatively small for the interdecadal time scale, the corresponding atmospheric response in the midlatitude is relatively small.

The SST variation in the midlatitude for the interdecadal time scale, however, is relatively large in spite of the smaller wind variation. This can be explained as follows: the interdecadal variation of the ocean subsurface at the midlatitude suggests spin-up of the subtropical gyre (Fig. 16) in response to the atmospheric circulation at the mid-high latitudes (Fig. 14b), remotely forced by the interdecadal variation of the tropical SST. Since spin-up time of the ocean in response to the atmospheric forcing is longer at the higher latitudes, the midlatitude ocean responds more to slowly varying forcing of interdecadal time scale than to forcing that quickly changes its sign in the ENSO period. We speculate that the subtropical gyre, spun-up by the interdecadal time scale forcing, affects the SST variation, which is expected to be larger than that for the ENSO time scale.

If the local SST anomaly in the midlatitude was controlling the variation of the extratropical atmospheric circulation, it is natural to consider that atmospheric response becomes large for interdecadal time scale whose SST anomaly in midlatitude is relatively large. However, the model result is contrary to that. It is suggested, therefore, that interdecadal variation of the tropical ocean plays a controlling role on the atmospheric circulation variability in the extratropics. This is consistent with the results from analyses of the observations and atmospheric model experiments by Lau and Nath (1994) and Graham et al. (1994).

It is proposed by Trenberth and Hurrell (1994) that a positive feedback of the SST anomaly at the midlatitudes, influencing the midlatitude's atmospheric circu-

lation to sustain or enhance the SST anomaly, is large for the interdecadal time scale. Latif and Barnett (1994) also claimed that interaction between the subtropical gyre circulation in the North Pacific and the Aleutian Low is important for interdecadal variability in the Pacific. They argued that decadal variability in the North Pacific is primarily attributed to coupled interactions in the midlatitudes. In contrast, our model result indicates significant influence of the tropics on the midlatitudes.

To elucidate the cause of interdecadal variation of the tropical ocean is also an important theme. Some possible mechanisms that determine the time scale of the interdecadal variation in the tropical Pacific are considered: (1) interaction between the tropics and the midlatitude in an air-sea coupled system, (2) subharmonics of the ENSO itself. The present study, we believe, demonstrates that further careful experiments and analyses with the coupled GCM will be effective ways to pursue these subjects.

Acknowledgements. The authors thank their colleagues in the Climate Research Department and the Oceanographical Research Department of the Meteorological Research Institute for informative discussions. The present study was performed as a part of the special project on the prediction of global warming of the Japan Meteorological Agency. A part of the study was also supported by the Center for Global Environmental Research/National Institute for Environmental Studies.

References

Arakawa A, Schubert WH (1974) Interaction of a cumulus cloud ensemble with the large-scale environment, part I. J Atmos Sci 31:674–701

Cubasch U, Hasselmann K, Höck H, Maier-Reimer E, Mikolajewicz U, Santer BD, Sausen R (1992) Time-dependent greenhouse warming computations with a coupled ocean-atmosphere model. Clim Dyn 8:55–69

Graham NE (1994) Decadal-scale climate variability in the tropical and North Pacific during the 1970s and 1980s: observations and model results. Clim Dyn 10:135–162

Graham NE, Barnett TP, Wilde R (1994) On the roles of tropical and midlatitude SSTs in forcing interannual to interdecadal variability in the winter northern hemisphere circulation. J Clim 7:1416–1441

Hellermann S, Rosenstein M (1983) Normal monthly wind stress over the world ocean with error estimates. J Phys Oceanogr 13:1093–1104

Horel JD, Wallace JM (1981) Planetary-scale atmospheric phenomena associated with the Southern Oscillation. Mon Weather Rev 109:813–829

IPCC (1990) Climate change, The IPCC Scientific Assessment. Houghton JT, Jenkins GJ, Ephraums JJ (eds) Cambridge University Press, Cambridge 365 pp

Kashiwabara T (1987) On the recent winter cooling in the North Pacific (in Japanese). Tenki 34:777–781

Kitoh A, Noda A, Nikaidou Y, Ose T, Tokioka T (1995) AMIP simulations of the MRI GCM. Pap Meteorol Geophys 45:121–148

Lacis AA, Hansen JE (1974) A parametrization for the absorption of solar radiation in the Earth's atmosphere. J Atmos Sci 31:118–133

Latif M, Barnett TP (1994) Causes of decadal climate variability over the North Pacific and North America. Science 266:634–637

Latif M, Sterl A, Maier-Reimer E, Junge MM (1993) Climate variability in a coupled GCM. Part I: the tropical Pacific. J Clim 6:5–21

Lau N-C, Philander SGH, Nath MJ (1992) Simulation of ENSO-like phenomena with a low-resolution coupled GCM of the global ocean and atmosphere. J Clim 5:284–307

Lau N-C, Nath MJ (1994) A modeling study of the relative roles of tropical and extratropical SST anomalies in the variability of the global atmosphere-ocean system. J Clim 7:1184–1207

Levitus S (1982) Climatological Atlas of the World Oceans, NOAA Prof Pap 13, US Government Printing Office, Washington, D.C.

Manabe S, Stouffer RJ, Spelman MJ, Bryan K (1991) Transient responses of a coupled ocean-atmosphere model to gradual changes of atmospheric CO_2. Part I:annual mean response. J Clim 4:785–818

Meehl GA (1990) Seasonal cycle forcing of El Niño-Southern Oscillation in a global coupled ocean-atmosphere GCM. J Clim 3:72–98

Mellor GL, Durbin PA (1975) The structure and dynamics of the ocean surface mixed layer. J Phys Oceanogr 5:718–728

Mellor GL, Kantha L (1989) An ice-ocean coupled model. J Geophys Res 94:10937–10954

Mellor GL, Yamada T (1974) A hierarchy of turbulence closure models for planetary boundary layers. J Atmos Sci 31:1791–1806

Mellor GL, Yamada T (1982) Development of a turbulence closure model for geophysical fluid problems. Rev Geophys Space Phys 20:851–875

Miller AJ (1992) Large-scale ocean-atmosphere interactions in a simplified coupled model of the midlatitude wintertime circulation. J Atmos Sci 49:273–286

Miller AJ, Daniel RC, Barnett TP, Graham NE, Oberhuber JM (1994) Interdecadal variability of the Pacific Ocean: model response to observed heat flux and wind stress anomalies. Clim Dyn 9:287–302

Nagai T, Tokioka T, Endoh M, Kitamura Y (1992) El Niño-Southern Oscillation simulated in an MRI atmosphere-ocean coupled general circulation model. J Clim 5:1202–1233

Neelin JD (1991) The slow sea surface temperature mode and the fast-wave limit: analytic theory for tropical interannual oscillations and experiments in a hybrid coupled model. J Atmos Sci 484:584–606

Nitta T, Yamada S (1989) Recent warming of tropical sea surface temperature and its relationship to the Northern Hemisphere circulation. J Meteorol Soc Japan 67:375–383

Palmer TN, Shutts GJ, Swinbank R (1986) Alleviation of a systematic westerly bias in general circulation and numerical weather prediction models through an orographic gravity wave drag parametrization. Q J R Meteorol Soc 112:1001–1039

Philander SGH, Pacanowski RC, Lau NC, Nath MJ (1992) Simulation of ENSO with a global atmospheric GCM coupled to a high-resolution, tropical Pacific Ocean GCM. J Clim 5:308–329

Philander SGH, Yamagata T, Pacanowski RC (1984) Unstable air-sea interactions in the tropics. J Atmos Sci 41:604–613

Randall D (1976) The interaction of the planetary boundary layer with large-scale circulations. Ph. D. Dissertation, The University of California, Los Angeles, 247 pp

Rasmusson EM, Carpenter TH (1982) Variations in tropical sea surface temperature and surface wind fields associated with the Southern Oscillation/El Niño. Mon Weather Rev 110:354–384

Shibata K, Aoki T (1989) An infrared radiative scheme for the numerical models of weather and climate. J Geophys Res 94:14923–14943

Schopf PS, Suarez MJ (1988) Vacillations in a coupled ocean-atmosphere model. J Atmos Sci 45:549–566

Stockdale T, Anderson D, Davey M, Delecluse P, Kattenberg A, Kitamura Y, Latif M, Yamagata T (1993) Intercomparison of tropical ocean GCMs. TOGA Numerical Experimentation Group, WMO/TD-No. 545

Tokioka T, Yamazaki K, Yagai I, Kitoh A (1984) A description of the Meteorological Research Institute atmospheric general circulation model (MRI·GCM-I). Tech Rep 13 MRI, 249 pp

Tokioka T, Kitoh A, Nakagawa S (1993) Interactions between lower atmosphere and the ocean realized in a coupled atmosphere-ocean general circulation model. Ext Abstr Int WCRP Symp – Clouds and Ocean in Climate. 28 September–2 October 1992, Nagoya, 1.5–1.8

Tokioka T, Noda A, Kitoh A, Nikaidou Y, Nakagawa S, Motoi T, Yukimoto S, Takata K (1995) A transient CO_2 experiment with the MRI CGCM-quick report. J Meteorol Soc Japan 73:817–826

Trenberth KE (1990) Recent observed interdecadal climate changes in the Northern Hemisphere. Bull Am Meteorol Soc 71:988–993

Trenberth KE, Hurrell JW (1994) Decadal atmosphere-ocean variations in the Pacific. Clim Dyn 9:303–319

Watanabe T, Mizuno K (1995) Interdecadal variation of the subsurface temperature in the Pacific Ocean. Preprint Int Workshop Numerical Prediction of Oceanic Variations, March 1995, JMA, Tokyo, 223 pp

Yagai I, Yamazaki K (1988) Effect of the internal gravity wave drag on the 12-layer MRI GCM January simulation. Rep 12 Proc WGNE Workshop on Systematic Errors in Models of the Atmosphere, 19–23 September 1988, Working Group on Numerical Experimentation, Toronto, 8 pp

Yamagata T, Masumoto Y (1992) Interdecadal natural climate variability in the Western Pacific and its implication in global warming. J Meteorol Soc Japan 70:167–175